



# Utilization of plant-derived Myricetin molecule coupled with ultrasound for the synthesis of gold nanoparticles against breast cancer

Uma Priya Mohan<sup>1</sup> · Bhaskaran Sriram<sup>2</sup> · Theivendren Panneerselvam<sup>3</sup> · Sankarganesh Devaraj<sup>1</sup> · Davoodbasha MubarakAli<sup>2,4</sup> · Pavadai Parasuraman<sup>5</sup> · Ponnusamy Palanisamy<sup>6</sup> · Adhvitha Premanand<sup>1</sup> · Sankarganesh Arunachalam<sup>1</sup> · Selvaraj Kunjiappan<sup>1</sup>

Received: 28 December 2019 / Accepted: 14 April 2020 / Published online: 28 May 2020  
© Springer-Verlag GmbH Germany, part of Springer Nature 2020

## Abstract

Phytochemical mediated synthesis of nanoparticles has gained great interest in the field of cancer therapeutics. We attempted a simple and stable synthesis of gold nanoparticles (AuNPs) with Myricetin (Myr) adopting ultrasound-assisted method. Further, we evaluated anticancer activity of the synthesized nanoparticles. The physico-chemical properties of biosynthesized Myr-AuNPs were characterized by UV-visible spectrophotometer, Fourier-transform infrared spectroscopy, X-ray diffraction, scanning electron microscopy, energy-dispersive X-ray spectroscopy, and particle size analysis. The study reports of Myr-AuNPs showed spherical-shaped particles with a size of < 50 nm. Stability of the particles was increased in various physiological media. Furthermore, the graph theoretical network analysis of Myr-AuNPs indicated that the probable binding with the mTOR is an effective target for breast cancer cells. In silico molecular docking study of Myr-AuNPs in human mTOR kinase was found to be strong binding. The IC<sub>50</sub> value of Myr-AuNPs was calculated as 13 µg mL<sup>-1</sup> against MCF-7 cell line. The AO/EB and DAPI stainings confirmed the anticancer activity by Myr-AuNPs-treated cells showed a good proportion of dead cells evidenced with formation of pro-apoptotic bodies. In addition, Myr-AuNPs exhibited depolarization of mitochondrial membrane potential and production of reactive oxygen species. This study proves that Myr-AuNPs holds great promise to use against breast cancer as a potent anticancer drug.

**Keywords** Myricetin · Gold nanoparticles · Apoptosis · Breast cancer · Cytotoxicity · MCF-7 cells

## Introduction

Breast cancer is one of the leading causes of death in women compared to other cancers (Sheffield 2019) and around 11.6

million new cases of breast cancer and 6.6 million deaths have been reported in 2018 (Bray et al. 2018). Although the primary diagnosis of breast cancer helps to achieve a moderate survival rate, distant metastasis hinders the actual survival rate

**Electronic supplementary material** The online version of this article (<https://doi.org/10.1007/s00210-020-01874-6>) contains supplementary material, which is available to authorized users.

✉ Sankarganesh Arunachalam  
sankarganesh@gmail.com

✉ Selvaraj Kunjiappan  
selvapharmabio@gmail.com

<sup>1</sup> Department of Biotechnology, Kalasalingam Academy of Research and Education, Krishnankoil, Tamil Nadu 626126, India

<sup>2</sup> School of Life Sciences, B.S. Abdur Rahman Crescent Institute of Science and Technology, Chennai, Tamil Nadu 600048, India

<sup>3</sup> Department of Pharmaceutical Chemistry, Saraswathi College of Pharmacy, NH-24, Anwarpur, Pilkhuwa, Hapur, Uttar Pradesh 245304, India

<sup>4</sup> Division of Bioengineering, Incheon National University, Incheon, Republic of Korea

<sup>5</sup> Department of Pharmaceutical Chemistry, Faculty of Pharmacy, M.S. Ramaiah University of Applied Sciences, M S R Nagar, Bengaluru, Karnataka 560054, India

<sup>6</sup> School of Mechanical Engineering, Vellore Institute of Technology, Vellore, Tamilnadu 632014, India

(Johnson et al. 2013). Studies attest that metastasis in breast cancer patients was more prevalent and observed in major organs and bones (Rygiel et al. 2017). Hitherto, chemotherapy remains the most effective treatment for breast cancer and metastasis. The adverse side effects associated with chemotherapy can be reduced simply by decreasing the dosage, and thus, chemotherapy is considered as the best modality (Pickus et al. 2000). On the other hand, decreased dosage limits therapeutic efficacy, and prolonged chemotherapy causes pronounced resistance. The specific cellular level changes caused by chemotherapy-induced resistance include target alteration, changes of metabolism and cell surface receptors, hindered apoptosis, and immune system evasion (Frank and Rosner 2012). These complexities in the signaling network help the breast cancer cells to escape from death induced by chemotherapeutics (Fodale et al. 2011).

There were many genes, enzymes, and molecules which were reported to be involved in protecting the cancer cells against chemotherapeutics (Krajka-Kuźniak et al. 2017). Eventually, these molecules and their signaling pathways were targeted for drug deliveries, which helped to suppress or inhibit the proliferation of cancer cells (Kunjiappan et al. 2018a). The above views are clearly indicating that treating a breast cancer patient thus becomes a challenge concern and treatment strategies for metastasis and breast cancer have become elusive. Therefore, we planned to use plants and their derived compounds because it has been traditionally used in the mitigation of many of the diseases, importantly cancer. Over 60% of currently used anticancer drugs are derived from plant source. The plants are possessing huge medicinal properties due to their bioactive compounds like alkaloids, flavonoids, sterols, terpenoids, and carotenoids. In addition, to enhance the quality of work, we utilized graph theoretical network analysis for identifying the synergistic binding of drugs to the ligands, thus becomes a selective approach to eliminate the cancer cells (Kunjiappan et al. 2018c). mTOR (mechanistic or mammalian target of rapamycin kinase) is one of the major targets, which is involved in cell growth, metabolism, and aging (Block et al. 2015). Among the therapeutic compounds, phytochemicals constitute a major class that includes flavonoids. In cancer cells, flavonoids were reported to modulate numerous signaling pathways and eventually hamper the proliferation and metastasis of cancer cells (N Syed et al. 2013). In particular, Myricetin, a flavonoid was found to inhibit the *PI3K/AKT/mTOR* signaling pathways and considered promising in cancer therapy (Kim 2017; Deeb et al. 2016; Yap et al. 2008). Myricetin (Myr, 3,5,7-trihydroxy-2-(3,4,5-trihydroxyphenyl)-4-chromenone) is widely distributed in various plants, fruits, vegetables, and medicinal herbs (Devi et al. 2015). Myr has a quercetin backbone with an additional hydroxyl group and it possesses enormous antioxidants through which it scavenges the free radicals and selectively targets the cancer cells (M Mates et al. 2011; Morales and

Haza 2012). We found Myr as a viable inducer of apoptosis (Kunjiappan et al. 2020). Chemically, Myr is insoluble in water (Yao et al. 2014); therefore, formulation and administration of Myr-based drug/emulsion are crucial.

The nano-based techniques are considered as an integral part of drug design and delivery (Chowdhury et al. 2017b) and among the various nanoparticles, gold nanoparticles (AuNPs) are highly selective against cancerous cells mostly due to their enhanced permeability and retention (EPR) effects (Ajnai et al. 2014; F Jiao et al. 2011). The synthesis of nanoparticles by high-intensity ultrasound results in cavitation wherein the formation, growth, and collapsing of bubbles are achieved by high pressure and high temperature and energy in the liquid medium (Deshmukh et al. 2019). Besides, cavitation bubbles produce intense local heating and high pressure in the liquid reaction mixture for a short period of time (Deshmukh et al. 2019). These transient, localized hot spots have an equivalent temperature of 5000 °C and pressure of 2000 atm that favor rapid reduction reaction (Kumar et al. 2016). Ultimately, the bubbles formed due to the cavitation yields a great amount of nanoparticles (Nasrollahzadeh et al. 2014). The present investigation involves the ultrasound-assisted green synthesis of Myr coupled with AuNPs for the effective therapeutic agents against breast cancer cells.

## Experimental section

### Materials

The chemicals, hydrogen tetrachloroaurate (III) hydrate  $\text{HAuCl}_4 \cdot 3\text{H}_2\text{O}$  (99.9%), Myricetin (Myr), acridine orange (AO), ethidium bromide (EB), 4',6-diamidino-2-phenylindole (DAPI), dichloro-dihydro-fluorescein diacetate (DCFH-DA), rhodamine 123, fetal bovine serum (FBS), 3-(4,5-dimethyl-2-thiazolyl)-2,5-diphenyl-tetrazolium bromide (MTT), Dulbecco's modified eagle's medium (DMEM), streptomycin, penicillin, and dimethyl sulfoxide (cell culture grade DMSO) were procured from Himedia laboratories Pvt. Ltd., Mumbai, India. A few other analytical grade chemicals and reagents were purchased from Thermo Fisher Scientific Ltd. Mumbai, India. All the solutions were prepared using deionized water.

### Ultrasound-assisted synthesis of gold nanoparticles

Gold nanoparticles were synthesized by a reduction method using Myr as a reducing and stabilizing agent (Kunjiappan et al. 2014). Briefly, 100 mL of 1 mM hydrogen tetrachloroaurate (III) hydrate solution was prepared. Myr (2 mg) was dissolved in 3 mL of methanol in a bath sonicator (Elma Ultrasonic Cleaner S100H, Mumbai, India). Later, the organic phase of Myr was added drop-wise to the aqueous phase of

hydrogen tetrachloroaurate (III) hydrate solution under ultrasonication (Sonics & Materials Inc., CT, USA) adopting the following parameters: 500 W, 20 kHz, pulse duty 50/10 s, amplitude 50% for 20 min followed by stirring at 600 rpm. The green synthesis of Myr-AuNPs was monitored through spectrophotometrically every 2 min for 20 min. Further characterization and anticancer activities were performed using the supernatant of Myr-AuNPs that was obtained by centrifuging the solution at  $6000\times g$  at 4 °C for 15 min.

### Physico-chemical characterization of Myr-AuNPs

Surface functional molecules of the Myr-AuNPs were detected and compared with Myr by FTIR (Shimadzu IR Tracer-100, FTIR spectrophotometer). The Myr-AuNPs powder was detected in XRD analysis at a voltage of 20 keV and a current of 30 mA with Cu K $\alpha$  1 radiation ( $I=0.1542$ ) in a 2-theta (degree) configuration (D8 Advance ECO XRD system with SSD160 1 D Detector). The zeta potential, average particle size, and distribution of the biosynthesized Myr-AuNPs were measured by Zetasizer (Nano ZS ver.7.03, Malvern Instrument, Worcestershire, UK). The SEM (Carl Zeiss EVO 18) was used to visualize the morphological features, whereas the TEM (TEM-JEOL model 2100) was used to assess the shape and size of the particles.

### Stability assessment of Myr-AuNPs

In vitro stability of Myr-AuNPs was assessed in various physiological media (10% NaCl, 0.5% BSA and 5% dextrose), acetate buffer solution pH 1.5, and phosphate buffer solution (PBS) at various pHs (3, 5, 6, 7.4, and 9), saliva, and simulated gastrointestinal fluids at room temperature (Kunjiappan et al. 2018b). Briefly, 1 mL of Myr-AuNPs was mixed with each physiological medium, PBS, saliva, and simulated gastrointestinal fluids followed by reading the absorbance after 48 h in a UV-visible spectrophotometer. Simulated gastrointestinal fluids were prepared according to Lazzari et al. (2012), and its composition and pH were presented in Supplementary Table S-1.

### Graph theoretical network analysis

A graph theoretical network analysis was performed by Kyoto Encyclopedia of Genes and Genomes (KEGG) database using Cytoscape software 3.7.1 (Theivendren et al. 2019) to recognize the roles of various genes in the mTOR (hsa04150) signaling mechanism, and resulted pathway is shown in Fig. 1. The analyzed network has 60 nodes and 78 edges based on centrality measures such as degree, closeness, eccentricity, eigen vector, and radiality. The measured value of degree (20), closeness (0.007686), eccentricity (0.267857), eigen vector (0.74402), radiality (18.74074), and stress (6948) has

indicated the threshold value of all the measures as well as notable node found in the network (Tables 1 and 2).

### In silico molecular docking

In silico molecular docking of targeted molecule (Myr) was accommodated by our previously published article (Kunjiappan et al. 2019c). The X-ray crystal structure of human mTOR kinase (PDB: 4JSV) was retrieved from the RCSB-PDB (Research Collaboratory for Structural Bioinformatics-Protein Data Bank). GLIDE program (v.11, Schrödinger, LLC, New York, 2016) was used in extra precision (XP) docking mode with the Glidescore and E-model scoring functions.

### In vitro cytotoxicity assay

MCF-7 cell lines (breast cancer cells) were obtained from NCCS, Pune, India, and maintained in DMEM medium containing 10% heat inactivated fetal bovine serum (FBS), 1% mixture of penicillin/streptomycin, and amphotericin B. In vitro cytotoxicity of Myr-AuNPs was performed against MCF-7 cancer cell lines, utilizing an MTT reagent-based colorimetric assay (Kunjiappan et al. 2019b). Briefly, MCF-7 cells were grown in 96-well plates ( $5 \times 10^3$  cells well<sup>-1</sup>) and incubated in DMEM (100  $\mu$ L) at 37 °C and 5% CO<sub>2</sub> for 24 h. Subsequently, the medium was replaced with fresh medium containing different concentrations of Myr-AuNPs (200, 150, 100, 50, 25, 12.5, 6.25  $\mu$ g mL<sup>-1</sup>) and incubated for 24 h. Later, the medium was removed and the cells were washed with PBS (0.01 M, pH 7.4). At the end of incubations, 100  $\mu$ L (5 mg mL<sup>-1</sup>) of 0.5% MTT solubilized in serum-free medium was added to each well and incubated for 4 h at 37 °C with 5% CO<sub>2</sub>. MTT fixative solution (isopropanol with 0.04 M HCl) of 100  $\mu$ L was added to the medium and removed after 4 h. ELISA plate reader (Bio-Rad, Model 680, Hercules, CA) was used to measure the absorbance at 570 nm for viable cells. The wells without Myr-AuNPs were marked as control. The percentage of cell viability was calculated using the following Eq. (1):

$$\text{Cell viability (\%)} = \text{At}/\text{Ac} \times 100 \quad (1)$$

where At and Ac are the mean absorbance of Myr-AuNPs-treated and control cells, respectively ( $n = 5$ ).

### Measurement of apoptosis by AO/EB (acridine orange/ethidium bromide) staining

Briefly, the MCF-7 cells ( $1 \times 10^5$ ) were seeded on 16 mm<sup>2</sup> cover slip followed by treatment with Myr-AuNPs for 48 h (Kunjiappan et al. 2019b). The cells were then washed twice

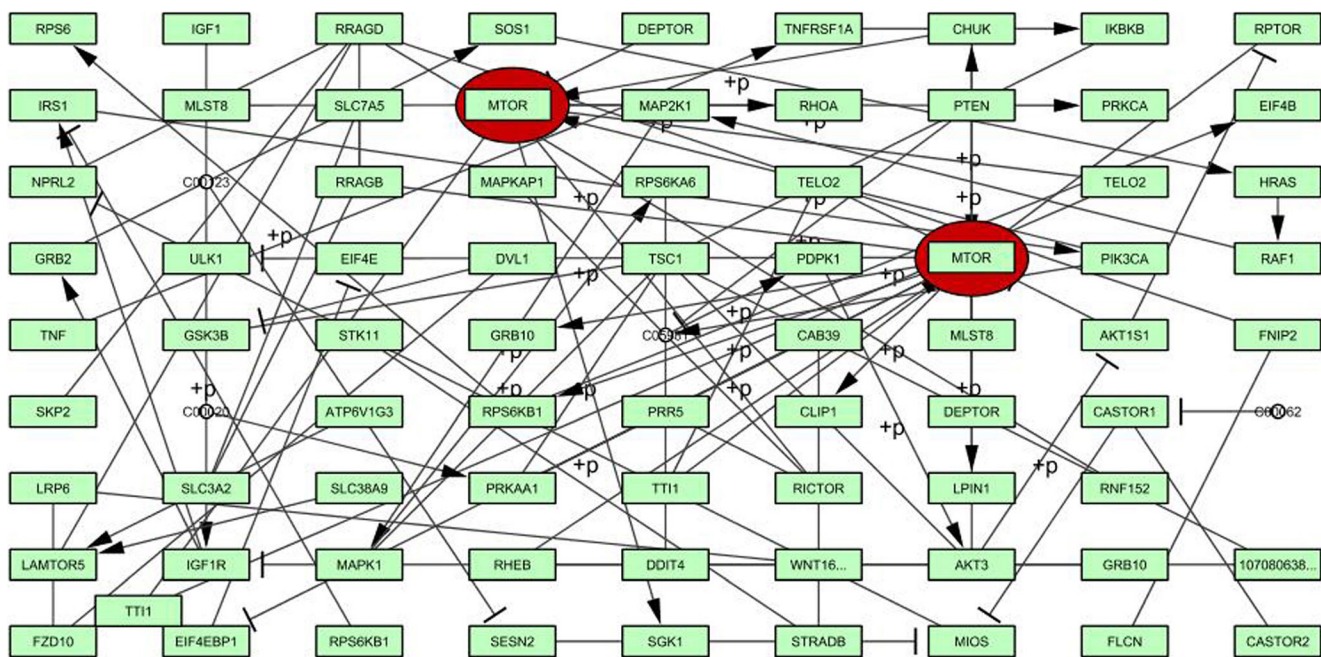


**Fig. 1** The signaling pathway of mTOR

with PBS and treated with AO and EB ( $10 \mu\text{L mL}^{-1}$  each) followed by incubation for 30 min. Subsequently, morphology of apoptotic cells was visualized under a fluorescent microscope (Carl Zeiss, Jena, Germany) at  $\times 40$  magnification (510–590 nm).

### Assay of mitochondrial transmembrane potential ( $\Delta\Psi\text{m}$ )

The  $\Delta\Psi\text{m}$  (changes of mitochondrial membrane potential) was measured according to the protocol reported elsewhere (Kunjiappan et al. 2018b). MCF-7 cells (density of  $1 \times 10^5$ ) were seeded onto 16 mm<sup>2</sup> coverslips placed in a 6-well plate and incubated at 37 °C for 4 h. The cells were treated with IC<sub>50</sub> concentration of Myr-AuNPs successively and then were rinsed using PBS. Subsequently, the cells were added with rhodamine 123 fluorescent dye ( $10 \mu\text{g mL}^{-1}$ ) for 1 h in dark

condition at 37 °C. Finally, fluorescence intensities were calculated using Spectramax M2 fluorescence spectrophotometer (Molecular devices, USA) at 480 nm (excitation wavelength) and 530 nm (emission wavelength). The reduced transmembrane potential of mitochondria in the treated cells was indicated by significant reduction in the uptake of rhodamine 123.

### DAPI (4',6'-diamino-2-phenylindole, 2HCl) staining

The morphological changes in the nuclear chromatin of the MCF-7 cells were detected by DAPI (DNA-binding fluorochrome) under fluorescence microscopy (Kunjiappan et al. 2019a). The MCF-7 cells ( $1 \times 10^5$  cells well<sup>-1</sup>) were grown in a cover slip of 24-well bottom dish and maintained in CO<sub>2</sub> incubator at 37 °C for overnight. The cultured cells were treated with IC<sub>50</sub> concentration of Myr-AuNPs and incubated for 48 h at 37 °C. The cells were washed with  $1 \times$  PBS buffer twice after the incubation and fixed with 4% paraformaldehyde solution for 30 min. Cells were incubated with DAPI for 5 min in the dark at room temperature followed by examination under fluorescent microscope (Carl Zeiss, Jena, Germany). The numbers of apoptotic cells were counted in the randomly selected fields.

### Determination of intracellular reactive oxygen species levels

Reactive oxygen species (ROS) generation was determined using dichloro-dihydro-fluorescein diacetate (DCFH-DA) fluorescence dye (Kunjiappan et al. 2015). MCF-7 cells ( $1 \times 10^5$  cells well<sup>-1</sup>) were seeded in 6-well culture plate and

**Table 1** The nodes and edges of influential protein (mTOR)

Centrality measures	Maximum	Mean	Minimum
Betweenness	5503.333	645.7051	130.75
Closeness	0.007686	0.002832024	0.001886
Degree	20	3.3076	2
Eigenvector	0.74402	0.072707	2.80E-04
Radiality	18.74074	7.881608104	5.82716049
Stress	6948	811.38	0
Nodes	60		
Edges	78		

**Table 2** The results of threshold parameter values of the network analysis

Rank	Gene	Betweenness	Closeness	Degree	Eccentricity	Eigenvector	Radiality	Stress
1	mTOR	5503.33	0.007686	20	0.267857	0.74402	18.7407	6948
2	RRAGB	2049	0.0037175	4	0.125	0.1886827	9.12346	2406
3	TSC1	1913.42	0.003663	8	0.125	0.1378706	9.07407	2240
4	RRAGD	1854	0.0032051	6	0.1111111	0.0604107	8.59259	2148
5	CHUK	1815.92	0.0039216	3	0.1428571	0.2039463	9.2963	2512
6	PRKAA1	1528.08	0.0038462	4	0.1428571	0.2026619	9.23457	1670
7	PIK3CA	862.583	0.0029326	3	0.1111111	0.028453	8.23457	1290
8	NPRL2	834	0.0026667	2	0.1	0.0148371	7.81481	960
9	AKT3	817.75	0.0035842	4	0.125	0.1396114	9	1348
10	MIOS	717	0.0022936	3	0.0909091	0.0038734	7.06173	822
11	IRS1	666.167	0.0025445	3	0.1	0.0074391	7.59259	948
12	GSK3B	572	0.0029155	2	0.1111111	0.0337253	8.20988	656
13	MAPK1	471.583	0.0029851	3	0.1111111	0.0439935	8.30864	540
14	IGF1R	468.583	0.002193	4	0.0909091	0.0020614	6.81481	646
15	DVL1	435	0.002457	2	0.1	0.0082496	7.41975	498
16	MAP2K1	353.083	0.0025575	2	0.1	0.0107632	7.61728	412
17	RPS6KB1	297	0.0032573	3	0.125	0.1663257	8.82716	338
18	RICTOR	296	0.0028011	3	0.1111111	0.0258751	8.03704	322
19	LAMTOR5	296	0.0025907	3	0.1	0.0156057	7.67901	338
20	CASTOR1	296	0.001992	3	0.0833333	0.0010006	6.24691	338
21	CAB39	294	0.003012	2	0.125	0.0495642	8.34568	312
22	IKBKB	294	0.0028902	2	0.1111111	0.0337185	8.17284	336
23	FZD10	294	0.0021368	2	0.0909091	0.0020176	6.66667	336
24	PDPK1	260.083	0.003012	2	0.1111111	0.0358407	8.34568	544
25	C05981	253.5	0.0027248	3	0.1	0.0156743	7.91358	510
26	RAF1	236.083	0.0022472	2	0.0909091	0.0026397	6.95062	288
27	EIF4EBP1	149	0.0032573	2	0.125	0.1569668	8.65432	170
28	FNIP2	149	0.0025641	2	0.1	0.0147276	7.62963	170
29	STRADB	149	0.0025063	2	0.1111111	0.0120834	7.51852	158
30	TNFRSF1A	149	0.0024155	2	0.1	0.0082203	7.33333	170
31	SESN2	149	0.0019881	2	0.0833333	9.44E-04	6.23457	170
32	LRP6	149	0.0018657	2	0.0833333	4.92E-04	5.82716	170
33	HRAS	140.583	0.0020284	2	0.0833333	6.74E-04	6.35802	188
34	GRB2	130.75	0.0020121	2	0.0833333	5.40E-04	6.30864	180
35	AKT1S1	128.583	0.0035461	3	0.1428571	0.2272316	8.96296	304
36	SOS1	98.9167	0.0018868	2	0.0769231	2.80E-04	5.90123	114
37	RHEB	77.1667	0.0034014	2	0.1428571	0.1647246	8.81481	104

incubated for 24 h at 37 °C with 5% CO<sub>2</sub>. The cells were then treated with IC<sub>50</sub> concentration of Myr-AuNPs and incubated for 48 h. Consequently, the cells were washed with 1× PBS for 15 min at 37 °C followed by labeling with DCFH-DA (20 μM). The suspension was kept on ice and filtered using a cell strainer (70 μM). In each well, the reaction mixtures were articulated and exchanged by PBS buffer (200 μL). The plates were then kept in dark on a shaker at room temperature for 10 min. The intensity of fluorescence was read at

475 nm ( $\lambda_{ex}$ ) and 525 nm ( $\lambda_{em}$ ) using a Spectramax M2 fluorescence spectrophotometer (Molecular devices, USA).

### Statistical analysis

MTT assay and ROS generation studies were performed in triplicate and the values were compared between control and treated cells using SPSS (v. 20.0, SPSS Inc., Chicago, IL, USA). We used one-way analysis of variance (ANOVA)

followed by Dunnett's test to evaluate the level of significance, where  $P > 0.05$  was considered significant. The results were expressed as mean  $\pm$  SD.

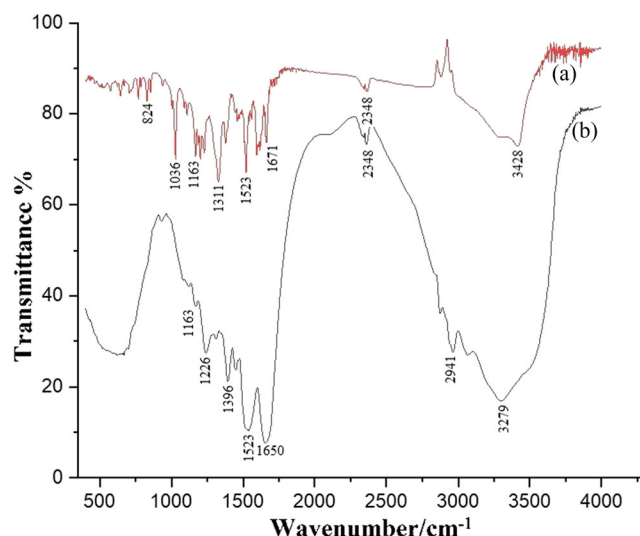
## Results

### Synthesis and characterization of Myr-AuNPs

Myr-AuNPs formation and stability were primarily confirmed by indicated color change (pale yellow to brown or cherry red), that occurred due to reduction of gold ions ( $\text{Au}^{1+}$  or  $\text{Au}^{3+}$ ) to neutral ( $\text{Au}^0$ ). Figure 2 represents the kinetics of the Myr-AuNPs biosynthesis and higher yields of stable Myr-AuNPs formed within 20 min. Further, the cherry red-colored solution expressed a sharp peak at 540 nm in UV-visible spectroscopy also confirmed the formation of Myr-AuNPs. Inset Fig. 2 (a) and (b) represents 1 mM hydrogen tetrachloroaurate (III) hydrate solution and Myr-AuNPs, respectively.

### Physico-chemical characterization

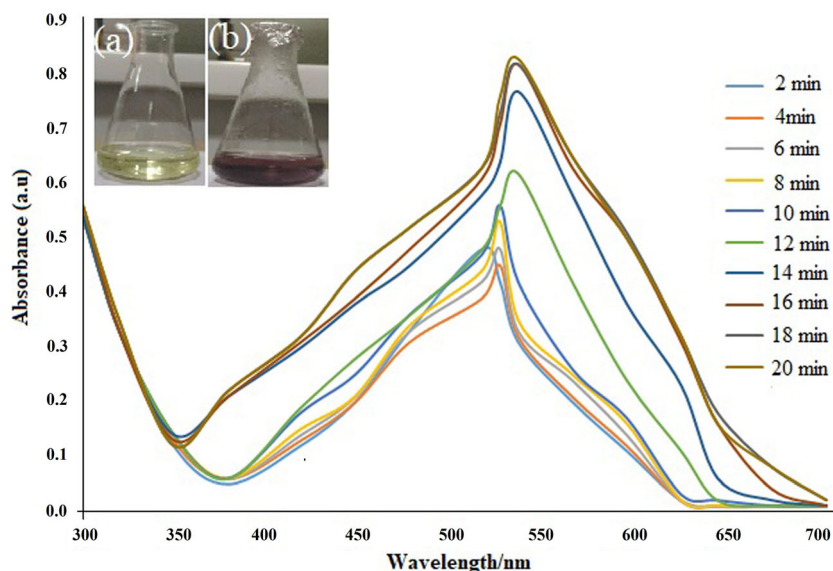
The FTIR spectrum of Myr-AuNPs (Fig. 3 (a)) exhibited a strong absorption peak at  $3279\text{ cm}^{-1}$  corresponding to O-H stretch of intermolecular hydrogen bonding. The peak at  $1650\text{ cm}^{-1}$  confirms the stretching vibrations of C-O group; another peak at  $1523\text{ cm}^{-1}$  confirms the presence of aromatic group. The band  $1396\text{ cm}^{-1}$  was assigned to the C-O-C vibrations. Interestingly, the observed peaks from spectra confirmed the presence of Myricetin (Fig. 3 (b)). In XRD analysis (Fig. 4), four diffraction peaks were observed ( $2\theta$ ) at  $38^\circ$ ,  $44^\circ$ ,  $65^\circ$ , and  $78^\circ$ . The observed peaks pattern corresponding to



**Fig. 3** FTIR spectra of Myricetin (a) and biosynthesized Myr-AuNPs (b)

lattice planes indexed to 111, 200, 220, and 311, which were identical with standard gold metal (Joint Committee on Powder Diffraction Standards-JCPDS file no. 65-8601). Bragg's reflections for Myr-AuNPs were found and confirmed based on the face-centered cubic (fcc) planes of pure gold element. The observed diffraction peaks suggest that Myr-AuNPs were crystalline in nature (Fig. 5 (a) and (b)). The average particle size of Myr-AuNPs was 66 nm and the measured zeta potential was  $-21.9\text{ mV}$ . SEM images revealed homogenous spherical-shaped Myr-AuNPs (Fig. 6 (a)–(c)). EDX spectrum of Myr-AuNPs exhibited strong signals for elemental gold (Fig. 6 (d)). TEM images revealed spherical-shaped particles between 30 and 66 nm size (Fig. 7 (a)–(c)). Further, the selected area electron dispersion (SAED) analysis exhibited that the Myr-AuNPs are predominantly

**Fig. 2** Kinetics of the formation of Myr-AuNPs (Inset figure (a) 1 mM hydrogen tetrachloroaurate (III) hydrate solution; (b) Myr-AuNPs)



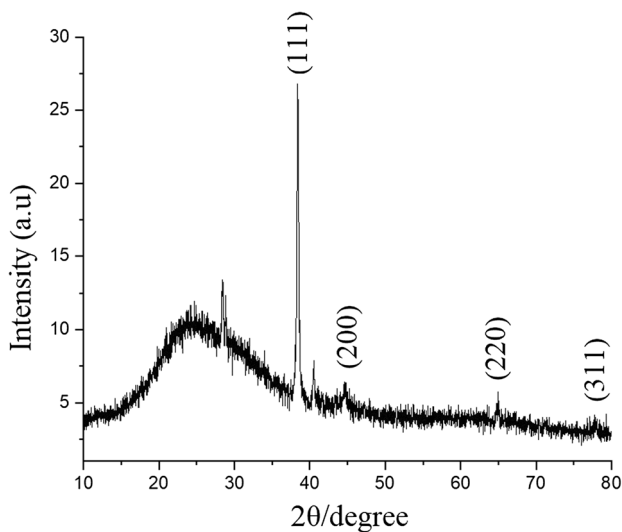


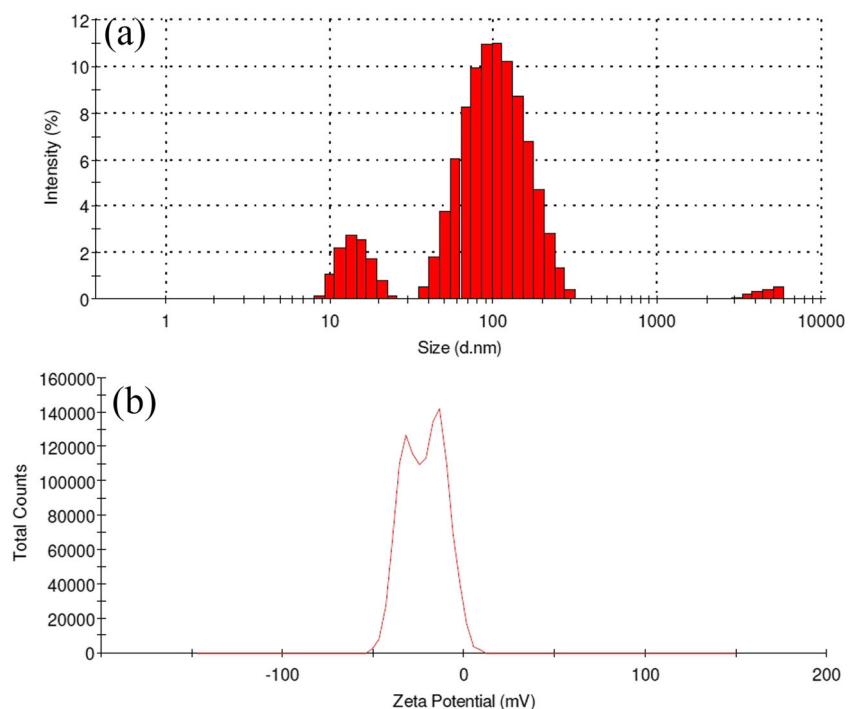
**Fig. 4** XRD pattern of lyophilized powder of Myr-AuNPs

single crystalline in nature. The spots are indexed based on fcc structure of Myr-AuNPs (Fig. 7 (d)).

### Stability studies

In Fig. 8, the  $\lambda_{\max}$  of Myr-AuNPs in different physiological solutions (10% NaCl (w/v), 0.5% BSA, and 5% dextrose (w/v)), acetate buffer solution pH 1.5, and phosphate buffer solutions (pH: 3, 5, 6, 7.4, and 9) was found to be 510 nm and 510–520 nm, respectively. In phosphate buffer solutions (pH 7.4 and 9), Myr-AuNPs displayed about 10 nm shifts in its  $\lambda_{\max}$ , whereas  $\lambda_{\max}$  of Myr-AuNPs in saliva and gastric

**Fig. 5** DLS measurement of average particle size of Myr-AuNPs (a); zeta potential of Myr-AuNPs (b)



intestinal and lysosomal fluids was found to be 530 nm. Promisingly, there was no absorbance shift between saliva and simulated gastrointestinal fluids. Altogether, these results demonstrated that Myr-AuNPs possess increased stability in various physiological media.

### In silico molecular docking analysis

In the present study, extra precision GLIDE docking procedure was validated by removing the inhibitor compound with human mTOR receptor. The docking result of Myr was found to be  $-7.79 \text{ kcal mol}^{-1}$ , and its interactions were found with ALA 1708, ARG 1709, LYS 1710, ILE 1711, and ASP 1712 of chain B of human mTOR kinase, eventually denote good binding of Myr with human mTOR kinase (Fig. 9). The interaction energy (van der Waals energy, electrostatic energy, and intermolecular hydrogen bonding) was calculated for each minimized complex.

### Cytotoxicity

We found  $69 \pm 1.57\%$  of cellular viability for  $6.25 \mu\text{g mL}^{-1}$  of Myr-AuNPs, whereas  $100 \mu\text{g mL}^{-1}$  of pure Myricetin showed only  $64.24 \pm 2.58\%$  cellular viability, and  $0.25 \mu\text{M}$  Paclitaxel showed  $50.12 \pm 1.26\%$  cellular viability (Fig. 10 (a)) and  $\text{IC}_{50}$  of Myr-AuNPs was found to be  $13 \mu\text{g mL}^{-1}$ , which produced effective morphological changes in MCF-7 cells, as shown in Fig. 10 (b) and (c).

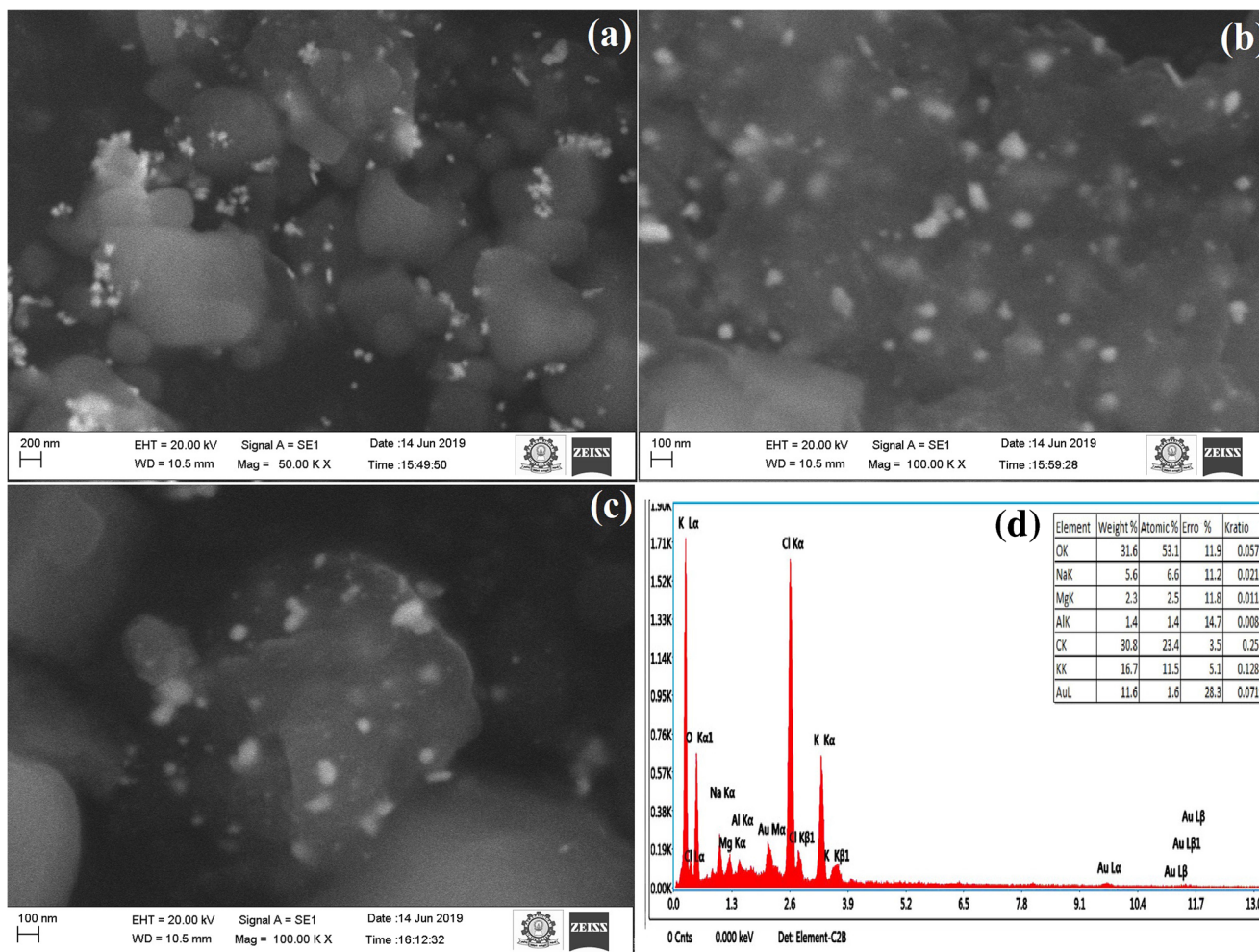


Fig. 6 SEM images of Myr-AuNPs (a)–(c); EDX pattern of Myr-AuNPs (d)

**Apoptosis**

The cells treated with Myr-AuNPs ( $13 \mu\text{g mL}^{-1}$ ) revealed early apoptotic bodies in orange color, and late apoptotic bodies (round or irregular shape with condensed nuclei and distorted membrane) in red color, whereas control MCF-7 cells displayed a normal nuclear morphology characterized by a diffused chromatin structure, therefore, visualized in green fluorescence (Fig. 11 (a) and (b)).

**Mitochondrial transmembrane potential ( $\Delta\Psi_m$ )**

The rhodamine 123 uptake was found to be higher in control cells compared to Myr-AuNPs ( $13 \mu\text{g mL}^{-1}$ ) treated cells (Fig. 12 (a) and (b)). The Myr-AuNPs greatly induced depolarization of the mitochondrial membrane potential and permeated the mitochondrial membrane via endocytosis that led to cell death.

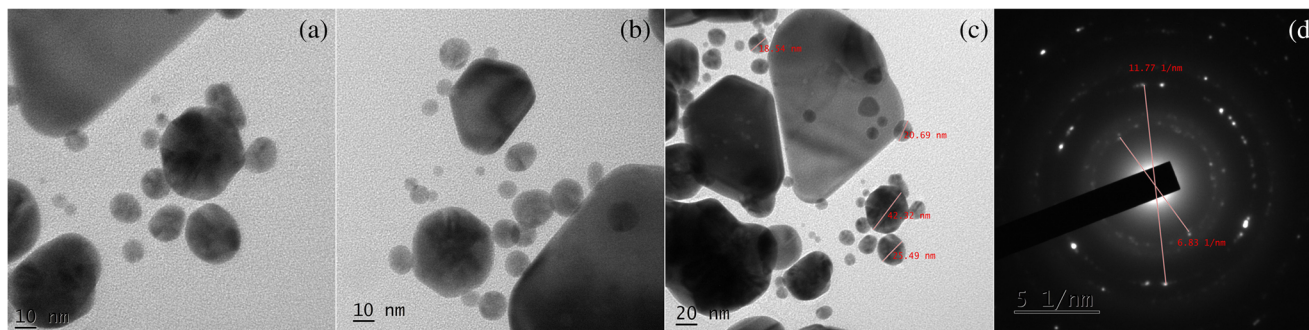
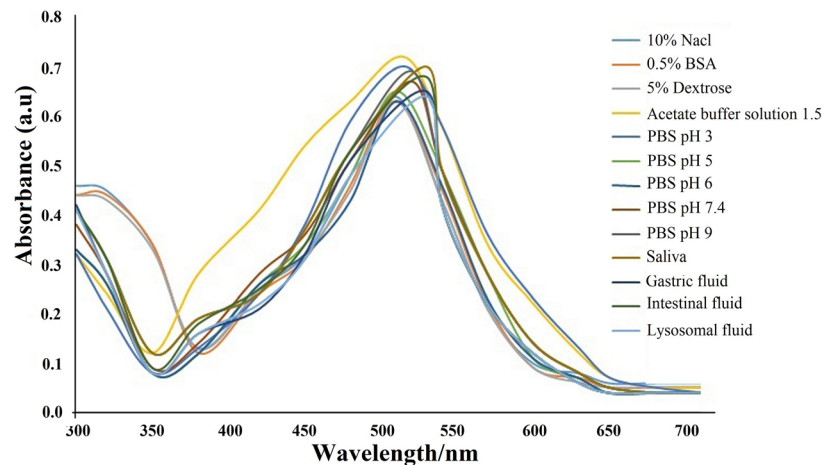


Fig. 7 HRTEM images of Myr-AuNPs (a)–(c). SAED pattern of synthesized Myr-AuNPs (d)



**Fig. 8** In vitro stability of Myr-AuNPs in physiological medium and various pH buffers



### DAPI staining

Figure 13 (a) and (b) demonstrated the morphology of DAPI stained MCF-7 cells (24 h) with and without AuNPs, respectively. The treatment of Myr-AuNPs ( $13 \mu\text{g mL}^{-1}$ ) with MCF-7 cells resulted in cell shrinkage, increased DNA condensation, and nuclear fragmentation, which denotes the characteristics of apoptotic morphology.

### ROS generation

The ROS generated in Myr-AuNPs ( $13 \mu\text{g mL}^{-1}$ )-treated MCF-7 cells was significantly higher ( $P < 0.05$ ) compared to control cells (Fig. 14). The increased ROS generation in Myr-AuNPs-treated cells might be responsible for oxidative stress.

### Discussion

AuNPs are widely utilized in disease diagnostics, targeted drug delivery, and treatments (Alanazi et al. 2010). Synthesis of biologically benign AuNPs using natural products is now getting more attention. In this study, we synthesized AuNPs using Myr, which acts both as reducing and stabilizing agent. The AuNPs synthesis by chemical, thermal, and electrochemical methods is time-consuming (Freitas de Freitas et al. 2018). It is apparent in the present study that

Myr-AuNPs were formed in a short period of time by ultrasonication-assisted method. Several lines of evidences point to the importance of ultrasound-assisted generation of AuNPs as one of the simple, efficient, alternative techniques to synthesize nanostructure in definite shape and size (Lee et al. 2012).

Synthesized Myr-AuNPs were characterized by UV-visible spectrophotometer at regular intervals. The peak intensity continuously increased (Fig. 2) during the synthesis of Myr-AuNPs due to rapid reduction of  $\text{HAuCl}_4$  and excitation of surface plasmon resonance (SPR). The SPR of AuNPs showed a single absorption peak at 540 nm, which is assigned to the dipole resonance of nanoparticles. Therefore, the observed SPR peak by Myr-AuNPs is in agreement with Mie theory (Singh et al. 2013b). The size of the nanoparticles was also related to the SPR absorbance band. Specifically, SPR band shifts toward higher wavelength as the size of nanoparticles increases, which was evident with the TEM analysis (Fig. 7 (a)–(c)).

Further, we evaluated the presence of the functional groups by comparing Myr and Myr-AuNPs. Further, the FTIR peaks were similar in the spectrum of both Myr-AuNPs and Myr. We have seen that there was a change of frequencies which might be credited to the contribution of the functional groups of those specific frequencies in the formation of the nanoparticles. The observed O-H stretching peak at  $3428 \text{ cm}^{-1}$  of Myr has moved to  $3279 \text{ cm}^{-1}$  after the formation of the nanoparticles. This demonstrates the reduction of  $\text{Au}^{3+}$  to  $\text{Au}^0$  with the

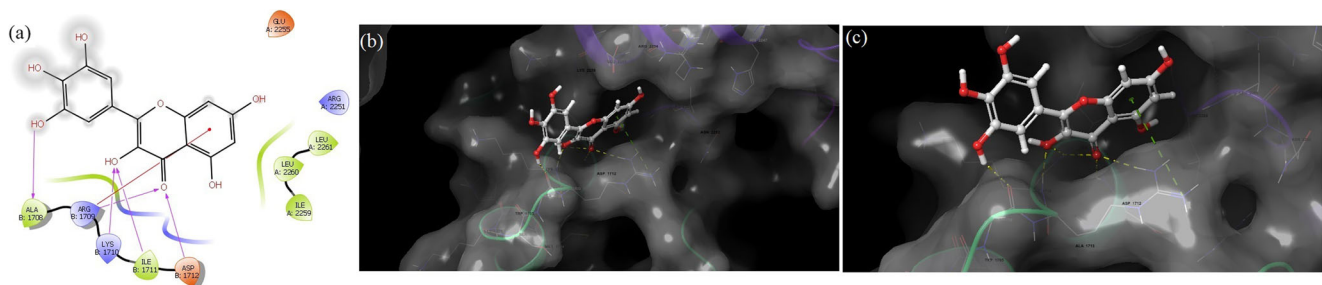


**Fig. 9** The molecular interactions of Myricetin with human mTOR kinase (PDB: 4JSV)

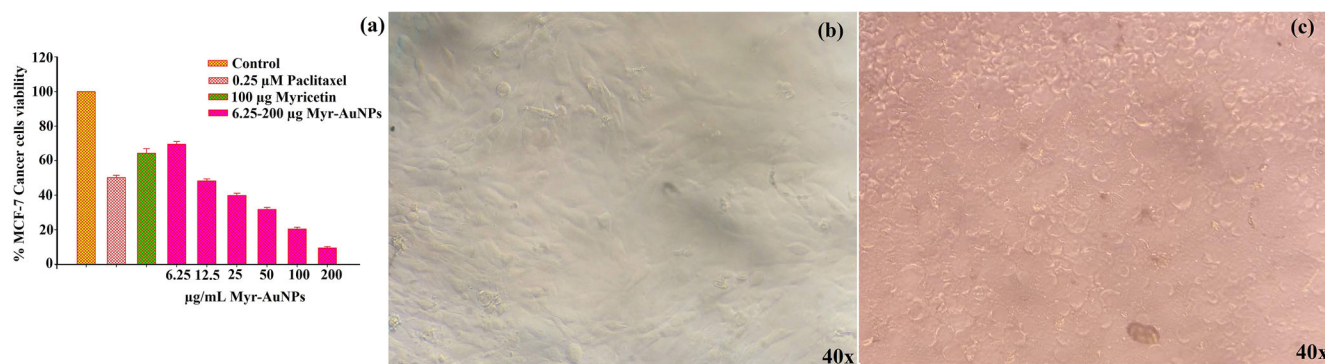


**Fig. 10** Cytotoxic activity of human adenoma breast cancer (MCF-7) cells using different concentrations of Myr-AuNPs after 24-h treatment. The percentage of apoptotic cells increased dose dependently. Values are

mean  $\pm$  standard deviation of triplicate measurements ( $p < 0.05$ ) (a); morphology of the control cells (b); and treated cells (c) observed using a phase contrast microscope

involvement of primary alcohol group of Myr. Similar result was observed in our previous study, where the biomolecules of *Marsilea quadrifolia* occupied the surface of AuNPs (Chowdhury et al. 2017a). The biosynthesized AuNPs exhibited standard Bragg reflections (111), (200), (220), and (311) of face-centered cubic (fcc) lattice. The strong intense diffraction at  $2\theta = 38^\circ$  peak shows the preferred growth orientation of zero valent Au (111) ions, which demonstrated that synthesized Myr-AuNPs were dispersed and single crystalline in nature. The single crystalline nanoparticles were further confirmed by SAED (selected area electron dispersion) pattern, and the observed results showed lattice fringes with bright circular rings demonstrating the gold ion. The SAED pattern of biosynthesized Myr-AuNPs confirmed the predominant presence of spherical shape and circular patterns corresponding to reflections of (111), (200), and (311). The zeta potential of Myr-AuNPs was found to be  $-21.9$  mV, and the negative charge indicates that Myr-AuNPs are highly stable (Singh et al. 2013a). Further, the surface charge of Myr-AuNPs indicates the penetrating potential of nanoparticles into the cells.

The AuNPs are used as a potential vehicle for delivery of variety of drugs (Webster et al. 2013). The stability of nanoparticles during storage condition is one of the key considerations in developing a therapeutic nano-formulation for cancer

treatment (Kesharwani et al. 2015). The stability of Myr-AuNPs was confirmed in various physiological media, PBS buffer, and simulated gastrointestinal fluids. There was no major shift in  $\lambda_{\max}$  of Myr-AuNPs upon treatment with any of the buffers treated with. We found higher stability for Myr-AuNPs in almost all the physiological medium that potentiates their longevity in blood plasma. The increased stability of Myr could be because of surface occupancy of Myr to the AuNPs.

The TEM micrograph of Myr-AuNPs showed well-dispersed particles without any aggregation. The size of the particles ranged from 30 to 66 nm. Further, the particles were anisotropic, with spherical, triangular, pentagonal, and hexagonal shapes. In line with our findings, Ramalingam et al. (2017) found TEM micrograph of gold nanoparticles in the size between 25 and 100 nm with spherical, triangular, hexagonal, pentagonal, rod, and truncated triangular shapes (Ramalingam et al. 2017). In this study, SEM images showed a combination of nanoparticles, which may be endorsed as the growth of nanostructures on different faces with respect to time. The size and shape of the nanoparticles depend on several factors, such as temperature, pH, sonication frequency, Myr concentration, and interaction with the functional groups of Myr (Jain et al. 2006; Sajanlal et al. 2011). Elemental analysis by energy-dispersive spectroscopy shows a strong peak

**Fig. 11** Apoptotic morphological variations of MCF-7 cells identified with AO/EB staining and observed using fluorescence microscope. (a) Control cells; (b)  $13 \mu\text{g mL}^{-1}$  of Myr-AuNPs for 48 h

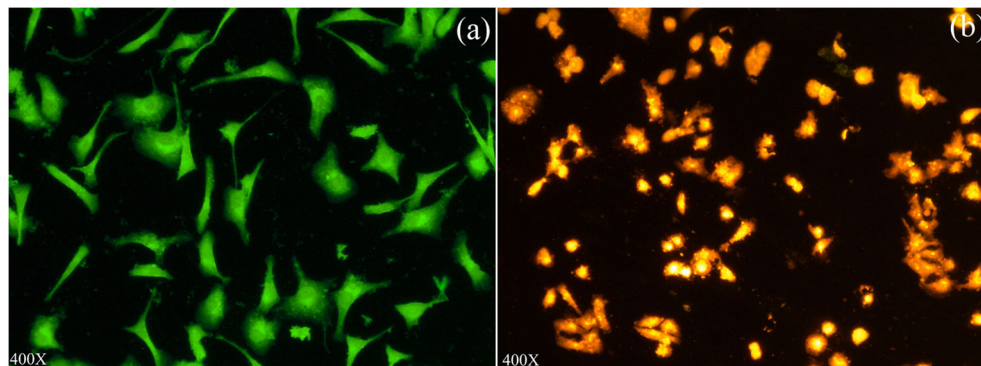
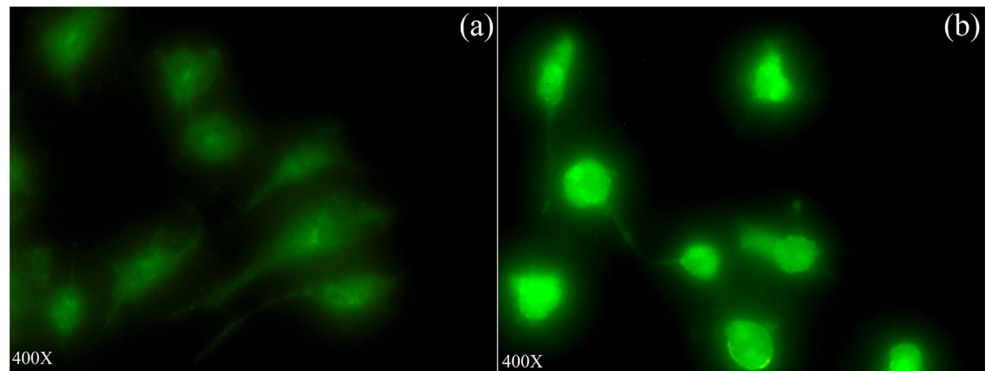


**Fig. 12** Effects of Myr-AuNPs on mitochondrial transmembrane potential in MCF-7 cancer cells. Control cells (a); notable loss of mitochondrial transmembrane potential on treated cells (b)



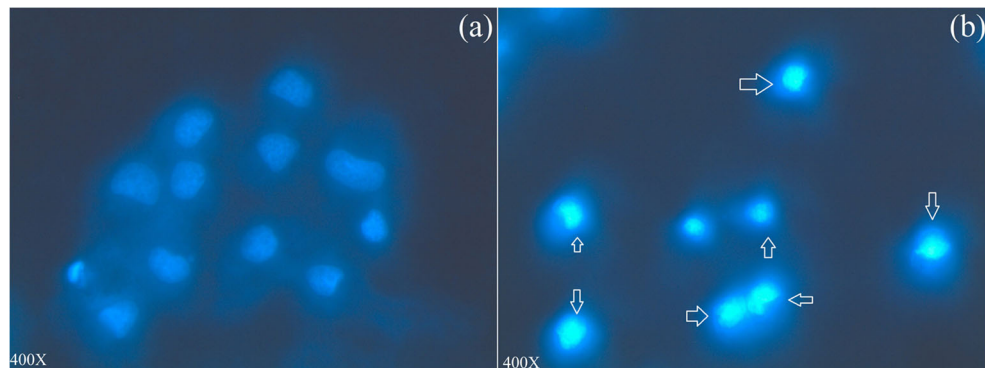
for gold along with weaker signals of other elements due to X-ray emission from Myricetin. The EDX spectrum confirmed the presence of Myr-AuNPs.

Many research reported that flavonoid-based AuNPs are effective against cancer, due to its nanodimension and shape that enhances the facilitated endocytosis in cells (Balakrishnan et al. 2017; Tiwari et al. 2015; Tripathi et al. 2015; Sreedharan et al. 2019; Raghavan et al. 2015). The size and shape of the nanoparticles thus become important in exerting cytotoxicity (Chithrani and Chan 2007). The nanoparticles of size up to  $\sim 50$  nm with a spherical shape were taken up by the cells faster and higher than other sizes and shapes (Sohaebuddin et al. 2010). We found in the present study that  $13 \mu\text{g mL}^{-1}$  Myr-AuNPs were effective in causing 50% death of cancer cells ( $\text{IC}_{50}$ ) in 24 h. Our results also established the dose-dependent anticancer activity of Myr-AuNPs against MCF-7 cells. Particularly,  $100 \mu\text{g mL}^{-1}$  of Myr-AuNPs showed  $20.38 \pm 0.98\%$  cell death, while  $25 \mu\text{g mL}^{-1}$  of Myr-AuNPs revealed  $39.9 \pm 1.25\%$  cell death. We articulate the anticancer activity of Myr-AuNPs to its spherical shape with smaller size. Further, we evidenced that the increased anticancer activity due to smaller size of Myr-AuNPs might provide a greater surface area of particles (Myr occupied) that eventually increases cancer cell death.

The findings of AO/EB staining revealed that Myr-AuNPs induce apoptosis in MCF-7 cells. Myr-AuNPs-treated cells revealed signs of apoptosis such as round- and irregular-

shaped cells with condensed nuclei, distorted membrane, and dead bodies. These results correlate well with our previous studies where MCF-7 cells upon treatment with  $0.1 \mu\text{g mL}^{-1}$  of Epirubicin-AuNPs encapsulated liposomes induced apoptosis as well as necrosis. The excessive generation of ROS is a critical event that might induce aging or senescence and apoptosis (Lemasters et al. 1998). In the present study, Myr-AuNPs-treated MCF-7 cells revealed a significant increase in ROS levels in MCF-7 cells as evidenced by experiment and figure no. This increased level of ROS in cancer cells might have enhanced the NPs to make the mitochondrial membrane permeable and aided to disturb the respiratory chain to induce p53-mediated intrinsic apoptosis pathway. It was reported that increased ROS level by anticancer agents leads to disruption of the homeostatic redox state and induces cellular genotoxicity that ends up with programmed cell death (Fulda et al. 2010), while the reduced level of ROS is involved in physiological condition as part of defense mechanisms and biological signaling process (Brieger et al. 2012). In spite of much technical advancement with the development of chemotherapeutic agents to battle against cancer, still mitochondria remain a viable therapeutic target. Mitochondria have several roles in important cellular functions, including the production of energy (adenosine triphosphate (ATP)),  $\text{Ca}^{2+}$  homeostasis, cell signaling, cell growth, cell cycle progression, and cell death (Elmore 2007). The mitochondrial membrane potential is generated by protons pumped into the

**Fig. 13** DAPI stained image of MCF-7 cancer cells. Control cells (a) and (b) treatment with Myr-AuNPs. Chromatin fragmentation is shown with arrow



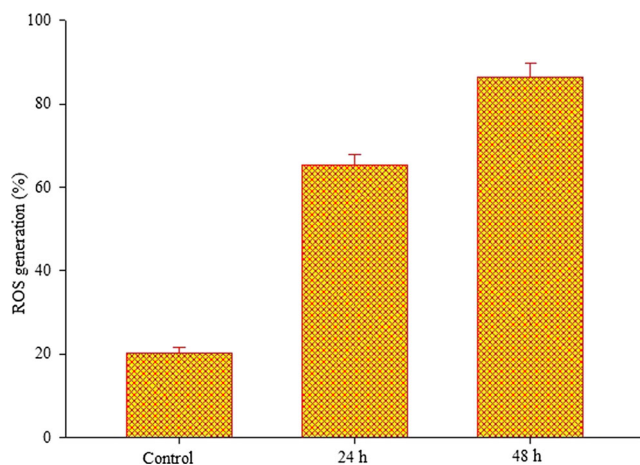


**Fig. 14** Effects of  $13 \mu\text{g mL}^{-1}$  of Myr-AuNPs on ROS generation (percentage of control value) in MCF-7 cancer cells. Results expressed as mean  $\pm$  standard deviation triplicate measurements ( $p < 0.05$ )

inner membrane space of the mitochondrion. The generation of energy occurs in the final step of oxidative phosphorylation, which results in ATP production by the electron transport chain. Mitochondrial modifications that arise during apoptosis include changes in mitochondrial transmembrane potential ( $\Delta\Psi\text{m}$ ) and ultrastructure as well as release of pro-apoptotic proteins such as cytochrome c from the intermembrane space.  $\Delta\Psi\text{m}$  is usually monitored by positively charged lipophilic fluorescent dye/probe (Rhodamine 123). In the present study, Myr-AuNPs-mediated cell death/apoptosis was observed by mitochondrial transmembrane potential damage/loss. Mitochondrial dysfunction was a significant oxidative damage due to higher level of ROS generation (Wang et al. 2014). Loss of  $\Delta\Psi\text{m}$  may occur due to opening of the so-called permeability transition pore complex (PTPC). PTPC is a supramolecular complex assembled at the junction of outer and inner mitochondrial membranes (Galluzzi et al. 2018; Bonora et al. 2015). Further, the efficiency of cell death/apoptosis was also closely monitored by changes of nuclear materials (DNA) by DAPI assay. DNA damage is one of the most important and endpoints and irreversible events in cell death (Elmore 2007). The Myr-AuNPs-treated MCF-7 cells were characterized by the typical morphological events of the nucleus such as nuclear fragmentation, and cell shrinkage which are linked with the apoptotic bodies of cells death.

## Conclusions

In the present investigation, we have demonstrated a simple and rapid method for development of Myr-induced AuNPs via ultrasound-assisted method for selective elimination of breast cancer cells. Myr acts as a reducing and stabilizing agent for AuNPs, and green synthesized Myr-AuNPs were relatively

stable in physiological solutions, PBS, saliva, and simulated gastrointestinal solutions. Further, the size, shape, and the morphological characteristics of biosynthesized Myr-AuNPs were studied and confirmed. The influence of ultrasound-assisted technique maintained uniform shape and favored the formation of nanoparticles (50 nm). Graph theoretical analysis and in silico molecular docking studies concluded that Myr-AuNPs have strong affinity to bind with human mTOR kinase. Myr-AuNPs mediated induction of apoptosis in breast cancer cells perhaps due to excessive ROS generation that caused oxidative stress and mitochondrial membrane potential loss. These potential benefits of Myr-AuNPs have opened up a new path for enhanced anticancer therapy for selective elimination of breast cancer cells.

**Acknowledgments** The authors are grateful to the Management of Kalasalingam University, Krishnankoil, India, for research fellowships and utilizing research facilities. We thank Mr. P. Kathirvel, Mr. V. Krishnaprabhu Technicians for FTIR and XRD analysis, Sir CV Raman-KS Krishnan International Research Center, Kalasalingam University, Krishnankoil, India, and SAIF, STIC, Cochin University, Cochin, Kerala, India, for TEM analysis. We also thank Prof. Z. Maciej Gliwicz, Ms. Ewa Babkiewicz, and Dr. Piotr Maszczyk, Department of Hydrobiology, Faculty of Biology, University of Warsaw, Warsaw, Poland, for timely help and support.

**Author contributions** UPM, SB, AP, PP, and SK conceived and designed the research. UPM, SB, AP, PP, DMA, SK, and TP conducted the experiments. KS, SA, SD, and DMA analyzed the data. KS, DMA, and TP wrote the manuscript. All authors read and approved the manuscript.

## Compliance with ethical standards

All procedures were performed in accordance with the National Institutes of Health Guidelines for the Care and Use of Laboratory Animals and were approved by the local animal protection committee.

**Ethics approval and consent to participate** Not applicable.

**Human and animal rights** No animals/humans were used for studies that are the basis of this research.

**Competing interests** The authors declare that there are no conflicts of interests.

## References

- Ajnavi G, Chiu A, Kan T, Cheng C-C, Tsai T-H, Chang J (2014) Trends of gold nanoparticle-based drug delivery system in cancer therapy. *J Exp Clin Med* 6(6):172–178
- Alanazi FK, Radwan AA, Alsarra IA (2010) Biopharmaceutical applications of nanogold. *Saudi Pharm J* 18(4):179–193
- Balakrishnan S, Mukherjee S, Das S, Bhat FA, Raja Singh P, Patra CR, Arunakaran J (2017) Gold nanoparticles-conjugated quercetin induces apoptosis via inhibition of EGFR/PI3K/Akt-mediated pathway in breast cancer cell lines (MCF-7 and MDA-MB-231). *Cell Biochem Funct* 35(4):217–231

- Block KI, Gyllenhaal C, Lowe L, Amedei A, Amin AR, Amin A, Aquilano K, Arbiser J, Arreola A, Arzumanyan A (2015) A broad-spectrum integrative design for cancer prevention and therapy. In: Seminars in cancer biology. vol Suppl. NIH Public Access, p S276
- Bonora M, Wieckowski MR, Chinopoulos C, Kepp O, Kroemer G, Galluzzi L, Pinton P (2015) Molecular mechanisms of cell death: central implication of ATP synthase in mitochondrial permeability transition. *Oncogene* 34(12):1475–1486
- Bray F, Ferlay J, Soerjomataram I, Siegel RL, Torre LA, Jemal A (2018) Global cancer statistics 2018: GLOBOCAN estimates of incidence and mortality worldwide for 36 cancers in 185 countries. *CA Cancer J Clin* 68(6):394–424
- Brieger K, Schiavone S, Miller FJ Jr, Krause K-H (2012) Reactive oxygen species: from health to disease. *Swiss Med Wkly* 142:w13659
- Chithrani BD, Chan WC (2007) Elucidating the mechanism of cellular uptake and removal of protein-coated gold nanoparticles of different sizes and shapes. *Nano Lett* 7(6):1542–1550
- Chowdhury A, Kunjiappan S, Bhattacharjee C, Somasundaram B, Panneerselvam T (2017a) Biogenic synthesis of *Marsilea quadrifolia* gold nanoparticles: a study of improved glucose utilization efficiency on 3T3-L1 adipocytes. *In Vitro Cell Dev Biol Anim* 53(6):483–493
- Chowdhury A, Kunjiappan S, Panneerselvam T, Somasundaram B, Bhattacharjee C (2017b) Nanotechnology and nanocarrier-based approaches on treatment of degenerative diseases. *Int Nano Lett* 7(2):91–122
- Deeb D, Gao X, Liu Y, Zhang Y, Shaw J, Valeriote FA, Gautam SC (2016) The inhibition of cell proliferation and induction of apoptosis in pancreatic ductal adenocarcinoma cells by verrucarin A, a macrocyclic trichothecene, is associated with the inhibition of Akt/NF- $\kappa$ B/mTOR pro-survival signaling. *Int J Oncol* 49(3):1139–1147
- Deshmukh AR, Gupta A, Kim BS (2019) Ultrasound assisted green synthesis of silver and iron oxide nanoparticles using fenugreek seed extract and their enhanced antibacterial and antioxidant activities. *Biomed Res Int* 2019:1–14
- Devi KP, Rajavel T, Habtemariam S, Nabavi SF, Nabavi SM (2015) Molecular mechanisms underlying anticancer effects of myricetin. *Life Sci* 142:19–25
- Elmore S (2007) Apoptosis: a review of programmed cell death. *Toxicol Pathol* 35(4):495–516
- Fodale V, Pierobon M, Liotta L, Petricoin E (2011) Mechanism of cell adaptation: when and how do cancer cells develop chemoresistance? *Cancer J (Sudbury, Mass)* 17(2):89
- Frank SA, Rosner MR (2012) Nonheritable cellular variability accelerates the evolutionary processes of cancer. *PLoS Biol* 10(4):e1001296
- Freitas de Freitas L, Varca GHC, dos Santos Batista JG, Benévolo Lugão A (2018) An overview of the synthesis of gold nanoparticles using radiation technologies. *Nanomaterials* 8(11):939
- Fulda S, Gorman AM, Hori O, Samali A (2010) Cellular stress responses: cell survival and cell death. *Int J Cell Biol* 2010:1–23
- Galluzzi L, Vitale I, Aaronson SA, Abrams JM, Adam D, Agostinis P, Alnemri ES, Altucci L, Amelio I, Andrews DW (2018) Molecular mechanisms of cell death: recommendations of the Nomenclature Committee on Cell Death 2018. *Cell Death Differ* 25(3):486–541
- Jain PK, Lee KS, El-Sayed IH, El-Sayed MA (2006) Calculated absorption and scattering properties of gold nanoparticles of different size, shape, and composition: applications in biological imaging and biomedicine. *J Phys Chem B* 110(14):7238–7248
- Jiao FP, Zhou YH, Chen XL, Yan B (2011) Cancer-targeting multifunctionalized gold nanoparticles in imaging and therapy. *Curr Med Chem* 18(14):2086–2102
- Johnson RH, Chien FL, Bleyer A (2013) Incidence of breast cancer with distant involvement among women in the United States, 1976 to 2009. *Jama* 309(8):800–805
- Kesharwani P, Banerjee S, Padhye S, Sarkar FH, Iyer AK (2015) Parenterally administrable nano-micelles of 3, 4-difluorobenzylidene curcumin for treating pancreatic cancer. *Colloids Surf B: Biointerfaces* 132:138–145
- Kim GD (2017) Myricetin inhibits angiogenesis by inducing apoptosis and suppressing PI3K/Akt/mTOR signaling in endothelial cells. *J Cancer Prev* 22(4):219–227
- Krajka-Kuźniak V, Paluszczak J, Baer-Dubowska W (2017) The Nrf2-ARE signaling pathway: an update on its regulation and possible role in cancer prevention and treatment. *Pharmacol Rep* 69(3):393–402
- Kumar B, Smita K, Sánchez E, Guerra S, Cumbal L (2016) Ecofriendly ultrasound-assisted rapid synthesis of gold nanoparticles using *Calothrix* algae. *Adv Nat Sci Nanosci Nanotechnol* 7(2):025013
- Kunjiappan S, Chowdhury R, Bhattacharjee C (2014) A green chemistry approach for the synthesis and characterization of bioactive gold nanoparticles using *Azolla microphylla* methanol extract. *Front Mater Sci* 8(2):123–135
- Kunjiappan S, Bhattacharjee C, Chowdhury R (2015) In vitro antioxidant and hepatoprotective potential of *Azolla microphylla* phytochemically synthesized gold nanoparticles on acetaminophen-induced hepatocyte damage in *Cyprinus carpio* L. *In Vitro Cell Dev Biol Anim* 51(6):630–643
- Kunjiappan S, Panneerselvam T, Prasad P, Sukumaran S, Somasundaram B, Sankaranarayanan M, Murugan I, Parasuraman P (2018a) Design, graph theoretical analysis and in silico modeling of *Dunaliella bardawil* biomass encapsulated keratin nanoparticles: a scaffold for effective glucose utilization. *Biomed Mater* 13(4):045012
- Kunjiappan S, Panneerselvam T, Somasundaram B, Arunachalam S, Sankaranarayanan M, Parasuraman P (2018b) Preparation of liposomes encapsulated Epirubicin-gold nanoparticles for tumor specific delivery and release. *Biomed Phys Eng Express* 4(4):045027
- Kunjiappan S, Panneerselvam T, Somasundaram B, Sankaranarayanan M, Parasuraman P, Joshi SD, Arunachalam S, Murugan I (2018c) Design graph theoretical analysis and in silico modeling of *Dunaliella bardawil* biomass encapsulated N-succinyl chitosan nanoparticles for enhanced anticancer activity. *Anti-Cancer Agents Med Chem* 18(13):1900–1918
- Kunjiappan S, Panneerselvam T, Govindaraj S, Parasuraman P, Baskararaj S, Sankaranarayanan M, Arunachalam S, Babkiewicz E, Jeyakumar A, Lakshmanan M (2019a) Design, in silico modeling, and functionality theory of novel folate receptor targeted rutin encapsulated folic acid conjugated keratin nanoparticles for effective cancer treatment. *Anti Cancer Agents Med Chem*
- Kunjiappan S, Theivendran P, Baskararaj S, Sankaranarayanan B, Palanisamy P, Saravanan G, Arunachalam S, Sankaranarayanan M, Natarajan J, Somasundaram B (2019b) Modeling a pH-sensitive Zein-co-acrylic acid hybrid hydrogels loaded 5-fluorouracil and rutin for enhanced anticancer efficacy by oral delivery. *3 Biotech* 9(5):185
- Kunjiappan S, Theivendren P, Pavada P, Govindaraj S, Sankaranarayanan M, Somasundaram B, Arunachalam S, Pandian SRK, Ammunje DN (2019c) Design and in silico modeling of Indoloquinoline incorporated keratin nanoparticles for modulation of glucose metabolism in 3T3-L1 adipocytes. *Biotechnol Prog*
- Kunjiappan S, Govindaraj S, Parasuraman P, Sankaranarayanan M, Arunachalam S, Palanisamy P, Mohan UP, Babkiewicz E, Maszczyk P, Sivakumar V (2020) Design, in silico modelling and functionality theory of folate receptor targeted Myricetin-loaded bovine serum albumin nanoparticle formulation for cancer treatment. *Nanotechnology* 31:155102
- Lazzari S, Moscatelli D, Codari F, Salmons M, Morbidelli M, Diomedea L (2012) Colloidal stability of polymeric nanoparticles in biological fluids. *J Nanopart Res* 14(6):920

- Lee J-H, Choi SU, Jang SP, Lee SY (2012) Production of aqueous spherical gold nanoparticles using conventional ultrasonic bath. *Nanoscale Res Lett* 7(1):420
- Lemasters JJ, Nieminen A-L, Qian T, Trost LC, Elmore SP, Nishimura Y, Crowe RA, Cascio WE, Bradham CA, Brenner DA (1998) The mitochondrial permeability transition in cell death: a common mechanism in necrosis, apoptosis and autophagy. *Biochim Biophys Acta Bioenergetics* 1366(1–2):177–196
- Mates MJ, Segura AJ, Alonso JF, Márquez J (2011) Anticancer antioxidant regulatory functions of phytochemicals. *Curr Med Chem* 18(15):2315–2338
- Morales P, Haza AI (2012) Selective apoptotic effects of piceatannol and myricetin in human cancer cells. *J Appl Toxicol* 32(12):986–993
- Nasrollahzadeh M, Ehsani A, Rostami-Vartouni A (2014) Ultrasound-promoted green approach for the synthesis of sulfonamides using natural, stable and reusable Natrolite nanozeolite catalyst at room temperature. *Ultrason Sonochem* 21(1):275–282
- Pickus O, Percy TB, Masih Farooqui M (2000) Results of a study to evaluate the use of Propax™ to reduce adverse effects of chemotherapy. *J Am Nutraceutical Assoc* 3(2):17–25
- Raghavan BS, Kondath S, Anantanarayanan R, Rajaram R (2015) Kaempferol mediated synthesis of gold nanoparticles and their cytotoxic effects on MCF-7 cancer cell line. *Process Biochem* 50(11):1966–1976
- Ramalingam V, Revathidevi S, Shanmuganayagam T, Muthulakshmi L, Rajaram R (2017) Gold nanoparticle induces mitochondria-mediated apoptosis and cell cycle arrest in nonsmall cell lung cancer cells. *Gold Bull* 50(2):177–189
- Rygiel KA, Drozd M, Bułaś L (2017) Care of cancer patients with liver and bone metastases—the place of pharmaceutical care in a balanced plan, focused on the patient's needs and goals. *Arch Med Sci* 13(6):1483–1492
- Sajanlal PR, Sreepasad TS, Samal AK, Pradeep T (2011) Anisotropic nanomaterials: structure, growth, assembly, and functions. *Nano Rev* 2(1):5883
- Sheffield D (2019) Assessing the effects of antioxidants on oxidative stress in triple-negative breast cancer cells via protein carbonylation. The University of Mississippi
- Singh DK, Jagannathan R, Khandelwal P, Abraham PM, Poddar P (2013a) In situ synthesis and surface functionalization of gold nanoparticles with curcumin and their antioxidant properties: an experimental and density functional theory investigation. *Nanoscale* 5(5):1882–1893
- Singh M, Kalaivani R, Manikandan S, Sangeetha N, Kumaraguru A (2013b) Facile green synthesis of variable metallic gold nanoparticle using *Padina gymnospora*, a brown marine macroalga. *Appl Nanosci* 3(2):145–151
- Sohaebuddin SK, Thevenot PT, Baker D, Eaton JW, Tang L (2010) Nanomaterial cytotoxicity is composition, size, and cell type dependent. *Part Fibre Toxicol* 7(1):22
- Sreedharan SM, Singh SP, Singh R (2019) Flower shaped gold nanoparticles: biogenic synthesis strategies and characterization. *Indian J Microbiol* 59(3):321–327
- Syed ND, Adhami MV, Imran Khan M, Mukhtar H (2013) Inhibition of Akt/mTOR signaling by the dietary flavonoid fisetin. *Anti-Cancer Agents in Medicinal Chemistry (Formerly Current Medicinal Chemistry-Anti-Cancer Agents)* 13(7):995–1001
- Theivendren P, Kunjiappan S, Govindraj S, Chandrasekarn J, Pavadai P, Saraswathy GR, Murugan I (2019) Graph theoretical analysis, insilico modeling and formulation of pyrimidine nanoparticles as p38 $\alpha$  MAP kinases inhibitors: a quantitative proteomics approach. *Drug Res* 69(02):100–110
- Tiwari P, Bawage S, Singh S (2015) Gold nanoparticles and their applications in photomedicine, diagnosis and therapy. In: *Applications of Nanoscience in Photomedicine*. Elsevier, pp 249–266
- Tripathi R, Shrivastav A, Shrivastav B (2015) Biogenic gold nanoparticles: as a potential candidate for brain tumor directed drug delivery. *Artif Cells Nanomed Biotechnol* 43(5):311–317
- Wang X, Wang W, Li L, Perry G, Lee H-g, Zhu X (2014) Oxidative stress and mitochondrial dysfunction in Alzheimer's disease. *Biochim Biophys Acta Mol Basis Dis* 1842(8):1240–1247
- Webster DM, Sundaram P, Byrne ME (2013) Injectable nanomaterials for drug delivery: carriers, targeting moieties, and therapeutics. *Eur J Pharm Biopharm* 84(1):1–20
- Yao Y, Lin G, Xie Y, Ma P, Li G, Meng Q, Wu T (2014) Preformulation studies of myricetin: a natural antioxidant flavonoid. *Die Pharmazie – Int J Pharm Sci* 69(1):19–26
- Yap TA, Garrett MD, Walton MI, Raynaud F, de Bono JS, Workman P (2008) Targeting the PI3K–AKT–mTOR pathway: progress, pitfalls, and promises. *Curr Opin Pharmacol* 8(4):393–412

**Publisher's note** Springer Nature remains neutral with regard to jurisdictional claims in published maps and institutional affiliations.